Diffusion limited hydration kinetics of millimeter sized salt hydrate particles for thermochemical heat storage

Journal of Energy Storage 47 (2022) 103554

Contents lists available at ScienceDirect

Journal of Energy Storage

journal homepage: www.elsevier.com/locate/est

Research Papers

Diffusion limited hydration kinetics of millimeter sized salt hydrate particles for thermochemical heat storage

Joey Aarts [a,b], Stan de Jong [b], Martina Cotti [a,b], Pim Donkers [c], Hartmut Fischer [d], Olaf Adan [b,d], Henk Huinink [a,b,*]

[a] Eindhoven Institute of Renewable Energy Systems, Eindhoven University of Technology, PO Box 513, Eindhoven 5600 MB, the Netherlands
[b] Transport in Permeable Media group, Department of Applied Physics, Eindhoven University of Technology, PO Box 513, Eindhoven 5600 MB, the Netherlands
[c] Cellcius, Horsten 1, 5612 AZ, Eindhoven
[d] TNO Materials Solution, High Tech Campus 25 Eindhoven, Netherlands

ARTICLE INFO

Keywords:
salt hydrates
thermochemical materials
heat storage
hydration kinetics
particles
K_2CO_3

ABSTRACT

Potassium carbonate is a promising salt for thermochemical heat storage. For an application mm-sized salt hydrate particles are manufactured to be loaded inside a reactor. The step towards larger particles is necessary to prevent a large pressure drop over the reactor bed during hydration/dehydration in a given air flow. Therefore, in this work a systematic study on the hydration kinetics of mm-sized disc shaped salt hydrate (K_2CO_3) particles is presented for the first time. The effect of density, primary particle size and driving force on the hydration kinetics was evaluated using a 1D diffusion model. The main conclusions are that the hydration kinetics of mm-sized salt hydrate particles is diffusion limited and that the particle density (porosity) and tortuosity are the main parameters controlling its performance. On the contrary, the primary powder size did not affect the particle performance in any way. It is shown that the calculated transport mechanism is unaffected by changes in driving force whereas the power output decreases with decreasing driving force. Lastly shape and size optimization is discussed which can possibly improve the hydration kinetics of salt hydrate particles in view of thermochemical heat storage. Since the particle hydration is expected to be similar for various other salts, the model from this work offers opportunities to predict and optimize particles made from different salts as well.

1. Introduction

The worldwide primary energy consumption has almost doubled in the period from 1980 till 2012 and is still increasing every year. A large part of this energy demand results from domestic space and water heating. In Europe space and water heating combined were responsible for up to 75% of the residential section's energy demand in 2010 [1,2]. To cope with this large, and ever increasing, energy demand in a sustainable way, several technologies are readily available. Such include the commonly known solar and wind energy. A few remarks can be made about these renewable energy systems. The major drawback of solar and wind energy is the inconsistent energy output which depends largely on the time of the year and location of the device [1,3,4].

This drawback can be overcome if one has a proper method of storing this energy. For example, during summer solar energy is readily available but the energy demand for space and water heating is low, while in winter times the opposite is true. Therefore, one needs a way of storing energy during the summer (peak in energy availability) which can be used during colder times (peak in energy consumption) for space and water heating.

To be able to accomplish this and account for the mismatch between energy availability and consumption, a new way of heat (energy) storage is under investigation using thermochemical materials (TCMs). These TCMs consist of salt crystals which can be hydrated to release energy in the form of heat. Dehydrating the material reverts this process and regenerates the starting material. The general chemical equation is written as

$$a(\text{salt}) + b(\text{reactant}) \rightleftarrows a(\text{salt})\cdot b(\text{reactant}) + Q \quad (1)$$

where a and b denote the stochiometric coefficients and Q the heat of reaction. Using these materials, energy can be stored under loss free conditions for longer times and is available on-demand. Recharging is done at times when energy is available in surplus, using for example

* Corresponding author.
E-mail address: h.p.huinink@tue.nl (H. Huinink).

https://doi.org/10.1016/j.est.2021.103554
Received 22 September 2021; Received in revised form 3 November 2021; Accepted 5 November 2021
Available online 17 November 2021

solar energy during the summer period [5,6].

One promising combination of salt and reactant proves to be potassium carbonate (K_2CO_3) and water. A screening of numerous salts resulted in this conclusion based on energy density, hydration/dehydration temperature and toxicity [7,8]. For this specific system the chemical equation is written as

$$K_2CO_3(s) + 1.5H_2O(g) \rightleftarrows K_2CO_3 \cdot 1.5H_2O\ (s) + Q. \quad (2)$$

On the powder level, the kinetics for potassium carbonate is already studied extensively. Gaeini and coworkers have investigated the effect of various parameters on the hydration kinetics of powdered K_2CO_3 samples. In their work a few milligrams of powder are used to investigate the chemical reaction rate [9]. Additionally, in recent work by Fisher and coworkers the hydration kinetics of K_2CO_3 powder is studied by using larger powdered sample masses in which diffusion limitations start to arise at higher conversions [10]. Fundamental research on the anhydrous to hydrous salt transitions has been performed recently by Sögütoglu and coworkers in two publications [11,12]. However, the interest in these solid-solid transition is already present for long times [13]. Cyclability and crack formation during cycling within small irregular K_2CO_3 particles has recently been investigated by Beving and coworkers [14].

To be able to use salt hydrates for seasonal heat storage these salt hydrates are put into a reactor bed trough which water vapor rich air is blown to hydrate the salt and release heat [7].

A detailed description of such possible reactor bed is given by Michel and coworkers [15]. Using salt hydrate powder directly results in a large pressure drops over the reactor bed which decreases the overall reactor performance [16]. Therefore, the salt powder is manufactured in the form of larger (mm-sized) particles. These mm-sized particles can be made in a well-defined shape consisting of dimensions of a few millimeters. These larger particles ensure better flowability of moist air through the thermochemical reactor bed and is expected to enhance the overall performance. Since the usage of such particle is necessary to cope with large pressure drops, understanding the performance and hydration kinetics is of great importance. This will allow for design and optimization of other shape stable mm-sized salt hydrate particles.

In contrary to the work on powder and small (<1 mm) irregular particles, this work is therefore focused on a different length scale and investigates the hydration kinetics of larger well defined shape stable mm-sized salt hydrate particles. For such particles an in depth and systematic investigations has not yet been performed investigating the influence of different parameters on the particle hydration kinetics, even though these particles are a crucial part in the overall reactor bed.

To be able to properly evaluate the energy output and performance of a thermochemical mm-sized particle, potassium carbonate in this work, several aspects affecting hydration must be understood. The key parameters affecting the hydration behavior are particle density (porosity), powder particle size and the thermodynamic driving force. In this work a 1D diffusion model is presented based on the shrinking core assumption, using the particle density as key input variable. The studied particles in this work were chosen to be flat and cylindrical of shape for mathematical ease of description. The outcome of this model, the effective diffusion coefficient, gives an insight in the hydration behavior of a mm-sized particle, independent of shape and used salt. Therefore, this model provides a handle for designing future thermochemical materials and predicting their kinetic behavior.

The outline of the paper is as follows. First, a 1D reaction front model based on the shrinking core model is discussed and applied to disc shaped salt hydrate particles. Next, the internal structure of these particles in investigated and afterwards primary powder reaction kinetics is linked to the potential existence of a front. The theoretical model is then validated experimentally using particles made from K_2CO_3. The effect of density (porosity), primary powder size and driving force of the hydration kinetics is investigated. Lastly, the kinetics of a 1D particle is extrapolated to 2D (infinite cylinders) and 3D particles (spheres).

2. Theory

In the following section first a generic reaction-diffusion model is discussed to describe the hydration kinetics in potassium carbonate particles. This model is then converted to a 1D front model which is then further simplified for easy parameterization. The different processes occurring on different length and time scales are shown in Fig. 1.

Two main processes will be in constant competition with each other, diffusion of water vapor towards the reaction front and reaction at the individual grains at this front. The ratio of both rates will determine how the overall hydration process proceeds.

The usage of a salt in general imposes a few limitations. The upper limitation for the used water vapor pressure is set by the deliquescence line (dotted line in Fig. 2 for K_2CO_3). Above this line, the salt goes into deliquescence and forms a saturated solution.

The lower limitation is set by the equilibrium line (red line in Fig. 2). Below this line the salt will exist as an anhydrate while above as hydrated material. This equilibrium line is calculated by calculating the equilibrium water vapor pressure at various temperatures using

$$p_{eq} = p^{\circ} \exp\left(-\frac{\Delta S^{\circ}}{R}\right) \exp\left(\frac{\Delta H^{\circ}}{RT}\right). \quad (3)$$

Herein p° [Pa] equals the standard pressure, ΔS° [J·mol^{-1}·K^{-1}] and ΔH° [J·mol^{-1}] are the standard entropy and enthalpy of the reaction at standard conditions. Obtained values calculated from literature thermodynamic data are ΔS°= -157 J·mol^{-1}·K^{-1} and ΔH° = 63.6 *k*J·mol^{-1} [17]. Sögütoglu and coworkers showed using cyclic TGA and DSC that the hydration enthalpy is independent on thermal history [8].

Even though hydration occurs when crossing the equilibrium line (dashed lines in Fig. 2), it is suggested to perform hydration experiments outside the metastable zone to avoid possible nucleation problems. Hydration proceeds by the formation of a mobile wetting layer of which the mobility depends on the water vapor pressure. Until a certain supersaturation is obtained, which represents the edge of the metastable zone, kinetics is hampered due to a nucleation barrier. Hydration does not start instantaneously and suffers from an induction time. Outside the metastable zone where the water vapor pressure is higher than the required supersaturation, nucleation occurs instantaneously. This metastability causes an overall performance drop since the achievable temperature lift before hydration stops is lower than the equilibrium hydration temperature. Due to the presence of a metastable zone below the hydration equilibrium line as well, the minimum dehydration temperature to start instantaneous dehydration is also higher than the equilibrium temperature. A more detailed description of metastability is given by Sögütoglu and coworkers [11].

In the following two sections two different approaches will be explained resulting in equations describing a reaction front in mm-sized cylindrical shaped particles. The first approach (section 2.1) is based on the reaction-diffusion equation, while the second approach (section 2.2) assumes that the chemical reaction itself is infinitely fast. In both approaches 1D transport behavior is assumed, and the resulting final equation are therefore only applicable to a 1D system (flat mm-sized cylinders in this work).

2.1. Generic reaction-diffusion model

Consider the equation for mass conservation of water vapor in the air, with Fickian diffusion through the completely homogeneous pore structure of an ideal reacting solid with constant (isotropic) diffusion coefficient:

$$\frac{\partial c}{\partial t} = D_{\text{eff}} \nabla^2 c - \frac{b \rho_{\text{anh}} (1 - \varepsilon_{\text{anh}})}{M_{anh}} \frac{dX}{dt}. \quad (4)$$

Here, c [mol·m^{-3}] is the water vapor concentration, t [s] is the time, x [m] is the spatial coordinate, ε_{anh} [−] is the porosity of the anhydrous

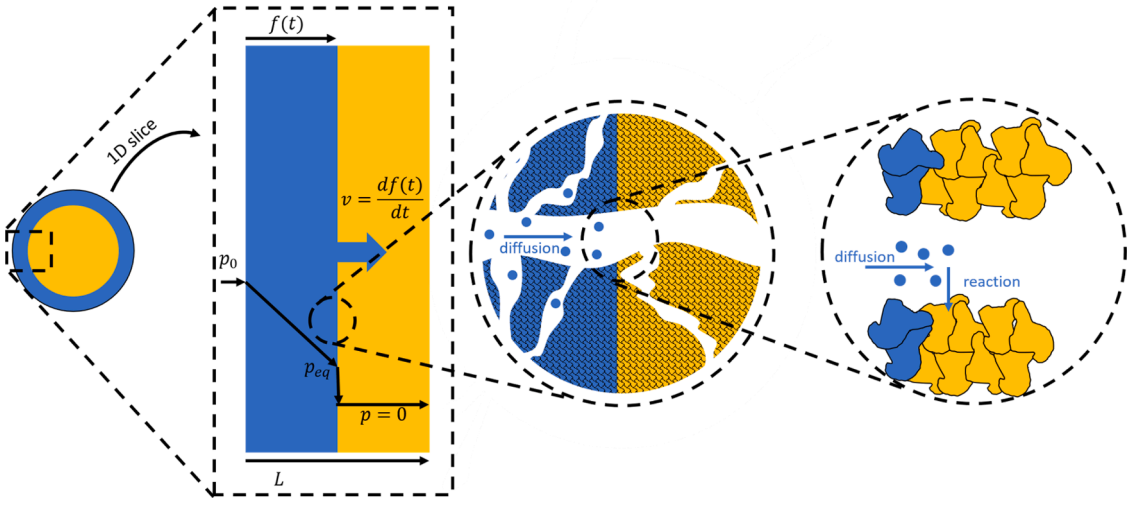

Fig. 1. Schematic representation of different processes occurring at different length and time scales inside a particle at the reaction front (assuming such a front exists). The blue parts resemble fully hydrated material while the orange parts are fully dehydrated. In the most left schematic, the pressure profile throughout a particle is shown. The outer and equilibrium water vapor pressures are denoted by p_0 and p_{eq} respectively. The front velocity is represented by v and equal to the change in front position $f(t)$ divided by the change in time t. The middle picture shows diffusion of water (blue spheres) toward the reaction front throughout the particle pore system. The right image shows the competition between water vapor transport toward the individual grains at the reaction front and reaction at the front.

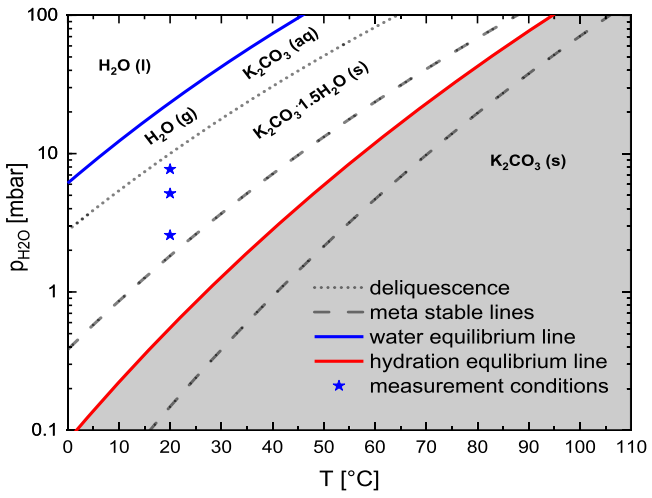

Fig. 2. Phase diagram of potassium carbonate including meta stable and deliquescence lines (dashed and dotted lines respectively) [11]. The red line represents the equilibrium line between the anhydrous (dark grey) and hydrated material. The blue line resembles the water liquid-gas line. The blue stars indicate the measurement conditions of the experiments in section 3. Conditions were chosen so that no deliquescence could occur, and nucleation problems are avoided.

phase, and D_{eff} $[m^2 \cdot s^{-1}]$ is the effective diffusion coefficient. b is a stoichiometric coefficient for reaction, ρ_{anh} $[\text{kg}\cdot\text{m}^{-3}]$ and M_{anh} $[\text{kg}\cdot\text{mol}^{-1}]$ are the density- and the molar mass of the pure anhydrous phase respectively, and X is the local conversion, defined as

$$X \equiv \frac{n_{\text{H}_2\text{O}}}{n_{\text{H}_2\text{O,max}}}. \tag{5}$$

Here, $n_{\text{H}_2\text{O}}$ $[\text{mol}\cdot\text{m}^{-3}]$ is the local water content in the material (loading), and $n_{\text{H}_2\text{O,max}}$ $[\text{mol}\cdot\text{m}^{-3}]$ is the maximum loading. In case the reaction rate is first order in concentration and primarily limited by the supply of water vapor, it can be approximated as

$$\frac{dX}{dt} = k_s \frac{M_{\text{anh}}}{b\rho_{\text{anh}}(1-\varepsilon_{anh})}\left(c - c_{eq}\right), \tag{6}$$

where k_s $[\text{s}^{-1}]$ is the reaction constant, and c_{eq} $[\text{mol}\cdot\text{m}^{-3}]$ is the equilibrium concentration for this reaction (Fig. 3). The system is considered isothermal in the following derivation, so the influence of thermal effects on the overall reaction rate is assumed to be negligible. Combining Eqs. (4) and (6) yields

$$\frac{\partial c}{\partial t} = D_{\text{eff}}\ \nabla^2 c - k_s\left(c - c_{\text{eq}}\right). \tag{7}$$

From Eq. (7) it is clearly visible that two different timescales play a role in the particle hydration. The first part on the right-hand side of the equation (containing D_{eff}) corresponds to diffusion and the second part (containing k_s) to reaction. Therefore, the second Dämkohler number for salt particle hydration can be identified, which is defined as the ratio between the typical time scales of diffusion τ_{D} [s] and reaction τ_{R} [s] [18]:

$$Da_{II} \equiv \frac{\tau_{\text{D}}}{\tau_{\text{R}}} = \frac{L^2 k_s}{D_{\text{eff}}}, \tag{8}$$

here L [m] is the typical length scale of the mm-sized particle. For small values of the Dämkohler number, reaction is slow compared to diffusion, and the hydration rate is limited primarily by the reaction rate. For large values of the Dämkohler number, diffusion is much slower than reaction, so the hydration is primarily limited by the diffusion of water vapor through the particle pores. In case the time scales of diffusion and reaction are both much smaller than the total hydration time, the system is quick to respond to changes in the water vapor concentration and can be considered in pseudo-steady state [19,20]. In this case Eq. (7) reduces to

$$\nabla^2 c - \frac{Da_{II}}{L^2}\left(c - c_{\text{eq}}\right) = 0. \tag{9}$$

The set of Eqs. (6) and (7) can be solved analytically, using the following boundary- and initial conditions:

$$X = 0,\ at\ t = 0, \tag{10}$$

$$c = c_0,\ at\ |\vec{r}| = \text{L}, \tag{11}$$

$$\vec{\nabla} c = 0,\ at\ |\vec{r}| = 0. \tag{12}$$

Here c_0 $[\text{mol}\cdot\text{m}^{-3}]$ is the outside water vapor concentration. For a full

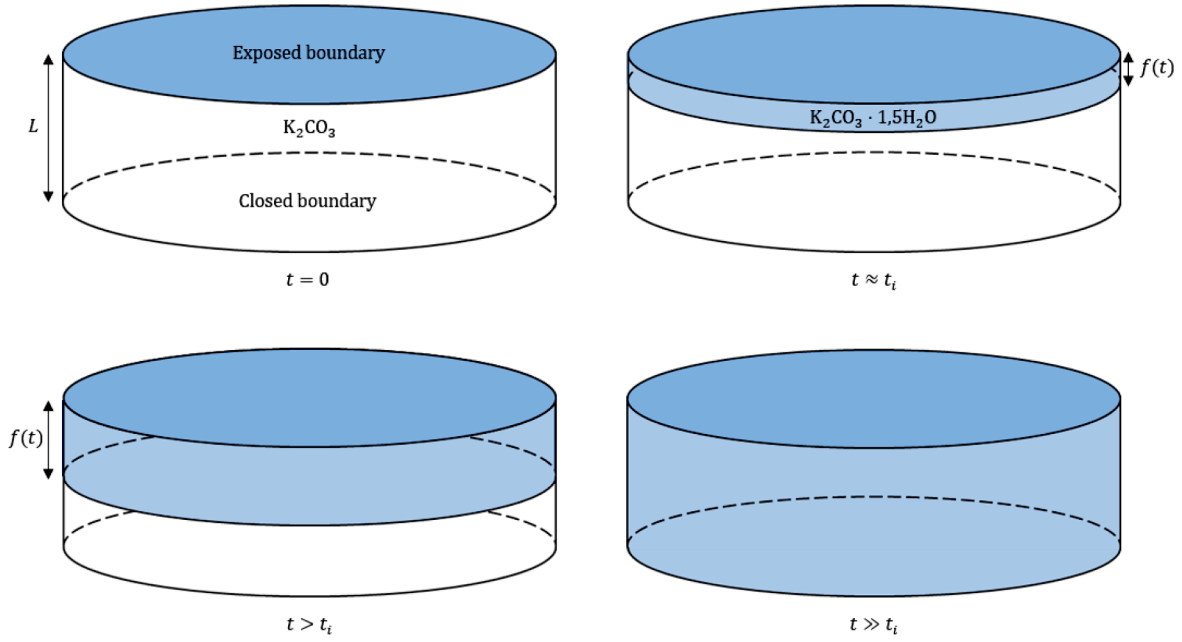

Fig. 3. An illustration of the proposed hydration process for a cylindrical potassium carbonate particle. The cylinder is exposed to water vapour at the top but sealed at the bottom. Initially the particle is completely in the anhydrous state (top left). After a brief initialization time, a thin layer at the exposed boundary of the cylinder is completely hydrated (top right). The hydration then proceeds with a reaction front travelling through the cylinder from top to bottom (bottom left). The particle is completely hydrated when the reaction front has reached the bottom of the cylinder (bottom right).

derivation, the reader is referred to the work of Szekely (1976) [21]. In this derivation, the hydration process is split up into two phases. First, there is an initialization phase, where no full conversion is reached throughout the particle. The initialization time t_i [s] required for a thin outer layer of the particle to be hydrated is

$$t_i = \frac{b\rho_{\text{anh}}(1-\varepsilon_{\text{anh}})}{k_s M_{\text{anh}}(c-c_{\text{eq}})}. \tag{13}$$

After the initialization period, the second phase begins. In this phase, the completely hydrated outer region of the particle moves inwards as hydration proceeds. This can be visualized as a hydration front travelling through the particle (Fig. 3). The dimensionless front position is defined as

$$\eta(t) \equiv \frac{f(t)}{L}. \tag{14}$$

Here, $f(t)$ [m] is the distance between the hydration front and the exposed edge of the particle.

From Szekely (1976) [21] the following (implicit) solution for the second phase of hydration ($t > t_i$) was obtained for a 1D geometry (flat plate), assuming a homogenous internal structure, with no significant surface layer effects:

$$X(f) = \eta + \frac{\tanh\left(\sqrt{Da_{II}}\,(1-\eta)\right)}{\sqrt{Da_{II}}}, \tag{15}$$

$$t(\eta) = t_i \cdot \left[\sqrt{Da_{II}}\cdot\eta\cdot\tanh\left(\sqrt{Da_{II}}\,(1-\eta)\right) + \frac{Da_{II}\cdot\eta^2}{2} + 1\right]. \tag{16}$$

Similar solutions for a 2D (cylinder) and 3D (sphere) geometry can be found in Szekely (1976) [21]. For large values of Da_{II} (i.e. high reaction rates) Eqs. (15) and (16) converge to

$$X(\eta) = \eta, \tag{17}$$

$$t(\eta) = t_i \cdot \frac{Da_{II}\cdot\eta^2}{2}. \tag{18}$$

Combining Eqs. (8), (13), (17), and (18) yields

$$X(t) = \sqrt{2\cdot\frac{M_{\text{anh}}\cdot(c_0-c_{\text{eq}})}{b\cdot\rho_{\text{anh}}\cdot(1-\varepsilon_{\text{anh}})}\cdot\frac{D_{\text{eff}}}{L^2}\cdot t}. \tag{19}$$

Using the ideal gas law, the concentrations can be expressed in terms of their corresponding partial pressures using

$$c = \frac{p}{RT}, \tag{20}$$

where p [Pa] is the water vapor pressure in air, R [J·mol^{-1}·K^{-1}] is the universal gas constant and T [K] the temperature. Combining Eqs. (14), (19) and (20) results in the following equation for the front position in a porous mm-sized cylindrical particle:

$$f(t) = \sqrt{\frac{2D_{\text{eff}}\,M_{\text{anh}}(p_0-p_{\text{eq}})}{RTb\rho_{\text{anh}}(1-\varepsilon_{\text{anh}})}\,t}, \tag{21}$$

where p_0 [Pa] is the water vapour pressure at the exposed boundary. When assuming negligible volume changes during the first cycle, Eq. (21) can be replaced with the following equation

$$f(t) = \sqrt{\frac{2D_{\text{eff}}\,M_{\text{anh}}A_0L(p_0-p_{\text{eq}})}{RTbm_{\text{anh}}}\,t}, \tag{22}$$

Here m_{anh} [kg] is the anhydrous mass of the particle and A_0 [m^2] the top surface which is exposed to water vapor.

2.2. Front description based on an infinitely fast reaction

Another way to derive Eq. (21) is by considering the reaction kinetics being fast from the start on and not rate limiting. This implies that any anhydrous material is instantly hydrated as it encounters water vapor. This results in the formation of an infinitely sharp reaction front, travelling through the particle (Fig. 3). Note that this corresponds to the situation where the Dämkohler number approaches infinity. The model derived here is commonly referred to as the 1D diffusion limited (D1) model for solid-state reaction kinetics [22], first proposed by Garner [23]. In the derivation, the isothermal assumption is applied again. The

flux of water vapor J_D [mol·m^{-2}·s^{-1}] through the pores of the particle is given by

$$\overrightarrow{J_D} = -D_{eff}\vec{\nabla}c. \tag{23}$$

Eq. (23) can also be written in terms of the water vapor pressure in air, using the ideal gas law (Eq. (20)):

$$\overrightarrow{J_D} = -\frac{D_{eff}}{RT}\vec{\nabla}p. \tag{24}$$

Assuming the volume of the particle remains constant during hydration, the velocity of the reaction front follows from the balance of water supply by diffusion and the amount of water that can react with a certain volume of K_2CO_3:

$$\frac{df(t)}{dt} = v\vec{n}\cdot\overrightarrow{J_D}, \tag{25}$$

$$v = \frac{M_{anh}}{b\rho_{anh}(1-\varepsilon_{anh})}. \tag{26}$$

Here, $\vec{n}$ [−] is the normal relative to the exposed surface of the particle. The movement of the reaction front follows from the water vapor pressure distribution in the particle, which can be determined from the constant flux condition in the completely hydrated part of the system where no water is reacting:

$$\nabla\cdot\overrightarrow{J_D} = 0, \tag{27}$$

$$\nabla^2 p = 0. \tag{28}$$

Assuming local equilibrium at the exposed surface and reaction front results in two boundary conditions for the water vapor pressure. The pressure at the exposed surface and reaction front must be equal to the outside (p_0) and equilibrium (p_{eq}) water vapor pressure, respectively.

The water vapour pressure distribution depends on the particle geometry. For a 1D geometry (flat plate) the cross-sectional area remains constant, resulting in the following linear water vapour pressure distribution:

$$p(r,t) = p_0 - (p_0 - p_{eq})\frac{r}{f(t)}. \tag{29}$$

Combining Eqs. (25) and (29) gives

$$\frac{df(t)}{dt} = \frac{D_{eff}M_{anh}(p_0 - p_{eq})}{RTb\rho_{anh}(1-\varepsilon_{anh})}\cdot\frac{1}{f(t)}. \tag{30}$$

This can be solved analytically again, yielding Eq. (21) for the front position over time.

3. Materials and methods

3.1. Particle manufacturing

Potassium carbonate sesquihydrate (confirmed by measuring the weight loss during drying, provided by Evonik Functional Solutions GmbH) has been milled (Fritsch planetary ball mill) and sieved into a 300-500 μm and 50-164 μm fraction. Powder of 10 μm (peak at 10 μm, d_{50} = 12.0 μm) was supplied by Evonik Functional Solutions GmbH and used directly without further treatment. Pressing of cylindrical particles was performed using a PO-Weber PW-40 2 column press. This resulted in cylindrical particles with a radius of 6.1 mm and variable heights (mm-sized) and densities (Fig. 4). The average particle height was 2.1 ± 0.1 *mm*. It was confirmed no water was pressed out of the particle during pressing by comparing the powder weight to the particle weight.

3.2. Density measurements

The density of particles was measured by dividing the weight of the particle by the geometrically measured volume (Mitutoyo digital caliper). The relative densities were calculated by dividing the measured density by the theoretical crystal density (2.18 g·cm^{-3} for hydrated and 2.43 g·cm^{-3} for anhydrous material) [24,25]. The absolute error in density measurements is estimated to be 0.01 (1% when the density is expressed in percentages).

$$\rho_{rel} = \frac{\rho_{measured}}{\rho_{theoretical}} = 1 - \varepsilon \tag{31}$$

3.3. Mercury Intrusion Porosimetry (MIP)

MIP was conducted on a Micromeritics AutoPore IV 9500 using a mercury pressure range from $7 * 10^{-4} \pm 0.1\%$ MPa to $228 \pm 0.1\%$ MPa. Hydrated particles were measured as they were pressed without further treatment. Anhydrous particles were dehydrated in an oven at 130 °C for at least 2 days before MIP measurements were conducted.

3.4. Scanning Electron Microscopy (SEM)

SEM samples were prepared by grinding away one half of the particle after which the grinded area was polished to smoothen the surface. Silver polish was added to increase the sample conductivity. Analysis was performed on a FEI Quanta 600 using low voltage and low vacuum measurements to reduce charge accumulation on the sample.

3.5. Thermogravimetric analysis (TGA)

TGA on salt hydrate powder was performed on a Mettler Toledo TGA/DSC3+. The sample was first dehydrated at 125 °C and zero water vapor pressure (gas flow 0.3 L·min^{-1}) for 90 minutes after which it was

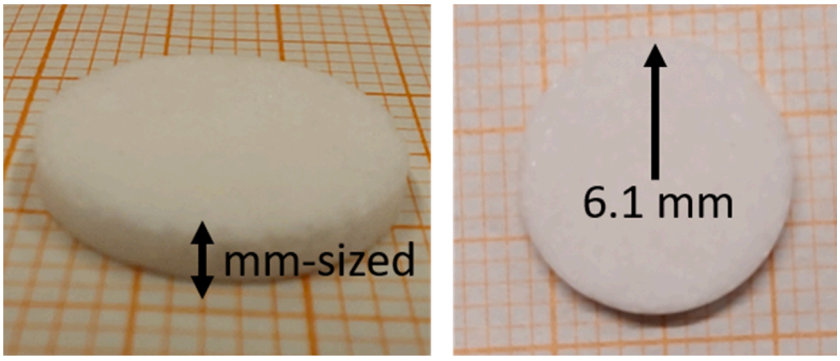

Fig. 4. Pictures of a K_2CO_3 particle with a mm-sized height and 6.1 mm radius (mm-paper background).

cooled to 20 °C. Here it was kept for 30 minutes at zero water vapor pressure to equilibrate the sample. Next hydration was performed by supplying 7.7 mbar (33% RH) of water vapor pressure at 20 °C and gas flow of 0.3 L·min^{-1}.

3.6. Kinetic measurements

Kinetic measurements were executed at 20 °C using saturated salt solutions inside a desiccator. The used salts are $MgCl_2$, CH_3COOK and LiCl generating a relative humidity (RH) above the salt solution of 33%, 22% and 11% respectively. To ensure a homogenous distribution of water vapor a small ventilator was placed inside the desiccator. Prior to being placed in a desiccator, the produced particles were fully dehydrated inside a 130 °C oven. Afterwards the weight loss was measured indicating complete dehydration. The dehydrated particles were placed inside the desiccator with one side (bottom) covered from water vapor. The particle weight was recorder by briefly taking it from the desiccator, weighting and putting it back with the same side down as before. The measurement conditions were chosen such that deliquescence conditions (43% RH at 20 °C) and nucleation problems are avoided. Note that 11% RH at 20 °C is outside the metastable zone (Fig. 2).

4. Results and discussion

Prior to the investigation of particle kinetics, the structural changes of a cylindrical particle and powder kinetics are elaborated which is followed by a brief discussion of possible edge effects. Next, the influence of particle porosity on the kinetic behavior is investigated followed by the effect of powder size and the effect of driving force. Lastly the kinetic behavior of different shapes is discussed.

4.1. Internal structure of pressed mm-sized particles

Since the structure of the fabricated cylindrical particles can influence the kinetic behavior, the effect of manufacturing pressure, powder size as well as dehydration on the structure is investigated. MIP measurements were conducted to determine the pore sizes of the particles.

First particles made from different powder sizes (10 μm and 300-500 μm) were produced using different manufacturing pressures. The cylindrical particles were pressed from hydrated powder and it was confirmed no water was lost during pressing by comparing the powder and particle weight. Eq. (31) was used to determine the relative density (porosity) of the particles. After complete dehydration at 130°C the density was measured again and the porosity and volume differences between the hydrated and anhydrous particle were calculated. From the results in Table 1 and Fig. 5, three main observations are made:

1 The relative density of the particle as produced (hydrated) depends on the applied pressure and the powder size.
2 The relative density of the dehydrated particle only depends on the original applied pressure but hardly depends on the powder size.
3 Particles made from smaller powder sizes have a larger initial volume decrease and smaller porosity increase upon dehydration

Two main reasons exist for the lower particle density (as produced in their hydrated state) for particles made from 10 μm base powder as seen in Fig. 5. The first reason is that smaller powder is less free flowing

Table 1
Structural changes between a fully hydrated and dehydrated particles for different particle sizes.

Powder size (μm)	Volume decrease (%)	Height decrease (%)	Porosity increase (%)
300-500	0.5-4.1	0.5-3.8	233-1287
10	6-8.1	1.9-4.4	172-344

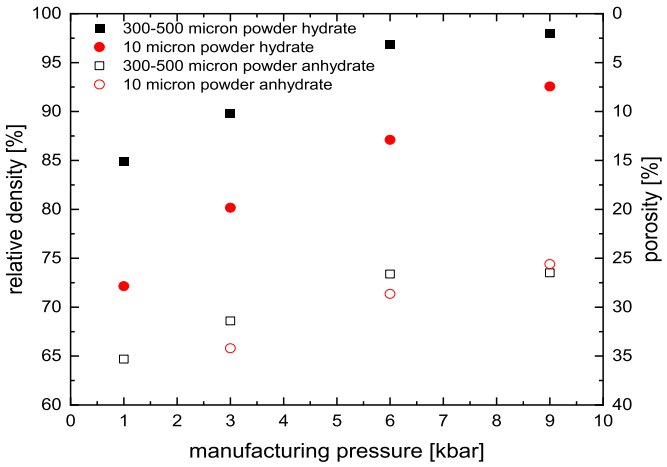

Fig. 5. Relative densities of cylindrical hydrous (as produced) and anhydrous K_2CO_3 particle made from different powder sizes at different manufacturing pressures.

compared to larger ones and will therefore pack less dense [26,27].

The second reason originates from the so-called rearrangement and fragmentation step [28]. This step results in breaking of the particles into smaller ones and rearranging those smaller particles to fit into the cavities created by larger particles. Since the powder with 300-500 μm particle size has a particle size distribution which will broaden due to fragmentation, rearrangement between the particles results in a more dense packing [29,30].

After dehydration it is observed that the relative density of the particles is largely independent of the powder size at a given manufacturing pressure. This is the result of the volume changes occurring during dehydration. When dehydrating, the grain volume within the mm-sized particle is expected to decrease due to the removal of water from the crystal lattice. Since the particle is constructed out of multiple grains, the total volume of the particles is also expected to decrease somewhat. The porosity is expected to increase as seen in Table 1 due to additional pore formation within the individual grains.

Since particles made from 300-500 μm powder are already more densely packed before dehydration (having lower porosity), there is less room to rearrange the particle internal structure into a smaller total volume. As a result of that, a large amount of volume created from removing water is contributing to the particle porosity. For the particle made from 10 μm powder the opposite is happening. Since these particles had a lower density when produced, the newly created volume by removing water is most probably used to rearrange the internal structure. As a result, the total volume of the particle decreases, and the effective porosity increase is smaller. Since the volume of these particles decreases more than those made from larger primary powder, the anhydrous volumes will become similar and with that also the density in their anhydrous state.

To get a more detailed insight into the precise structures of these pores, MIP measurements were performed on hydrated (directly after pressing) and anhydrous samples made from 300-500 μm base powder (Fig. 7). For the hydrated particles (directly after pressing) with the lowest density (82%), a broad peak with its highest value at 20 μm is observed. These pores mainly originate from the cavities in between the larger grains. For the particle with 91% density a bimodal pore volume distribution is found with peaks around 400 nm and 8 μm. The additional smaller pores result from the earlier mentioned fragmentation and rearrangement step, which broadens the width of the (primary powder) particle size distribution. The increased width of the distribution results in denser packing and smaller pores [30]. For the particle with 99% density only a peak in pore volume is found around 300 nm. Due to the very high pressure and with that a denser packing almost no cavities in

between larger grains remain, and only small pores are found.

SEM images performed on hydrated samples clearly show a more porous system with larger chunks of salt for a particle pressed at lower pressures, while the particle pressed at higher pressure shows a densely packed structure with fewer and smaller pores (Fig. 6).

MIP of the anhydrous particles shows an increase in pore volume at only small pore diameters for the particle with the highest density (98%). The particle with intermediate density (90%) shows an increase in the amount of small and large pores with a new peak forming around 2 μm resulting in a trimodal pore size distribution. For the particle with the lowest density (85%) the original peak at 20 μm is largely unchanged while 2 new peaks around 200 nm and 3 μm are formed. This results in a trimodal pore size distribution as well.

The formation of smaller pores during dehydration can be attributed to pore formation inside individual grains and possible shrinkage of these grains, reducing the size of the newly generated pores. Since the individual grains inside the particles are shrinking during dehydration, some pores which are already present in the hydrated state will grow in volume during dehydration. In addition, this can possibly counter the pore contraction during the overall particle shrinkage and is most probably responsible for the increase in volume contribution of the larger pores. Overall, the total pore volume increases with decreasing density and upon dehydration (Table 2).

Generally the porosity resulting from MIP measurements (on hydrous and anhydrous particles) was found to be lower than the geometrically calculated porosity (using Eq. (31), see Table 2). Two explanations for this observation exists:

1. Some pores are isolated and inaccessible by mercury during MIP.
2. Very small pores (a few nanometer) are inaccessible for mercury during the MIP experiments.

Pores which are inaccessible to mercury will not be used to compute the total pore volume and porosity when using MIP. The first type is a pore surrounded by salt. These pores are inaccessible to both mercury and water vapor. The second type of pore accessible for water vapor but not mercury are pores smaller than 5 nm (the limit of the MIP device). These pores do additionally have the potential to block of larger pores from mercury. The first type is expected to be less significant than the second type. Due to mercury not being able to fully penetrate the pore structure the found value using MIP differs significantly from the geometrical porosity. Therefore, we expect the geometrical porosity to be closer to the true porosity being accessible for water vapor.

For the sample in row three, Table 2, the MIP porosity seems to be greater than the geometric porosity. However, due to the absolute error of 1% in the geometric porosity (as mentioned in the experimental section) no significant difference can be observed.

4.2. Kinetics of primary powder and existence of a reaction front

To investigate the ratio of diffusion throughout the particle and reaction rate at primary grains, TGA experiments were performed on powders with different diameters (20 °C, 7.7 mbar (33% RH)). The TGA conversion for hydration for the 10, 50-164 and 300-500 μm fractions is shown in Fig. 8.

From the 10 μm powder TGA data, a reaction rate constant can be obtained from the initial slope of the conversion versus time graph. Fitting Eq. (6) to the TGA data resulted in a reaction rate constant k_s of 80.4 ± 0.1 s^{-1}. This data can now be used to compute the second Dämkohler number (Da_{II}) at different penetration depths and rate constants using Eq. (8) (Fig. 9). Since the reaction rate for a primary particle decreases over time, the Dämkohler number will as well until the reaction is no longer diffusion but reaction dominated. However, deeper into the particle at higher penetration depths, a lower reaction rate is still enough to maintain a diffusion limited reaction ($Da_{II} > 1$). This indicates that a reaction front can exist within a hydrating particle. The width of this front roughly corresponds to the penetration depth at which the colored Dämkohler lines intersect with the dashed line ($Da_{II} = 1$). The width of the reaction front will be determined by the water vapor diffusion coefficient within the porous particle. Lower diffusion coefficients will narrow the front while higher coefficients will broaden the front, as is illustrated in Fig. 9. For a D_{eff} of 1 mm^2·s^{-1} the front width will be 112 μm while a D_{eff} of 0.1 mm^2·s^{-1} reduces the width to 35 μm.

TGA measurements on the two larger powder fractions (50-164 and 300-500 μm) resulted in rate constants of 43.8 ± 0.1 s^{-1} and 33.3 ± 0.1 s^{-1} when fitting the initial slope (red and blue dashed line in Fig. 8) for the 50-164 and 300-500 μm fraction, respectively. A rate constant of 2.5 $\pm$0.1 s^{-1} is found when fitting the final slope of the 300-500 μm fraction (green dashed line in Fig. 8). For the 50-164 fraction a front width of 151 μm is expected for particles with a D_{eff} of 1 mm^2·s^{-1} and 48 μm when D_{eff} is 0.1 mm^2·s^{-1}. For the largest fraction (300-500 μm) a front width of 173 and 55 μm is predicted based on the initial reaction rates for D_{eff} is 1 mm^2·s^{-1} and D_{eff} is 0.1 mm^2·s^{-1} respectively. When computing a front width using the rate constant from the final slope of the 300-500 μm a front width of 632 and 200 μm is found for D_{eff} is 1

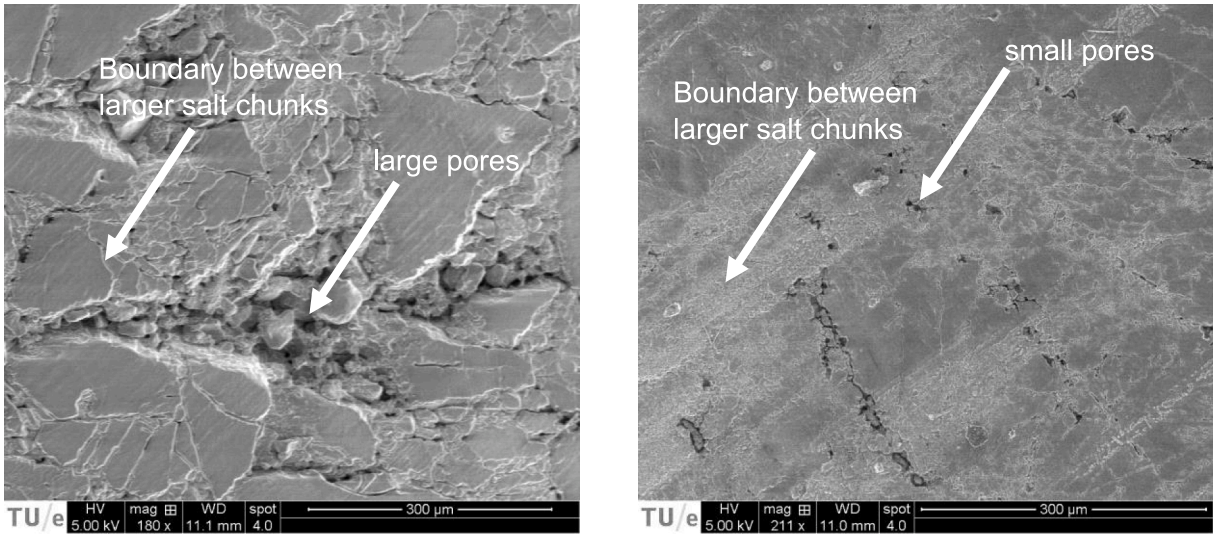

Fig. 6. SEM image of the cross-section of a hydrated particle made from 300-500 ***µm*** powder, pressed at low pressure with lower relative density (83%, left) and high pressure with higher relative density (96%, right).

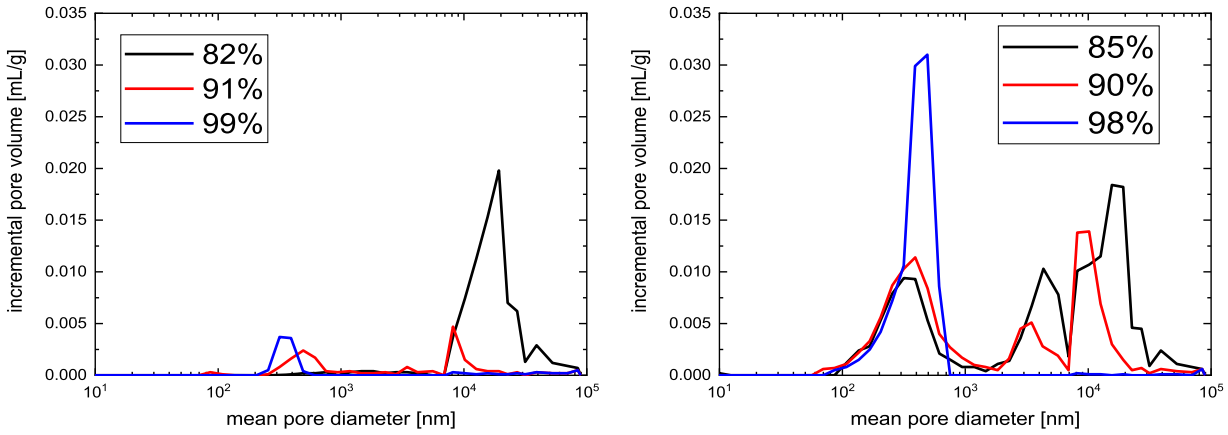

Fig. 7. MIP measurements on hydrated (left) and anhydrous particles (right) made from 300-500 ***μm*** powder with various relative densities in their hydrated state.

Table 2
Results obtained from MIP experiments. The geometrically calculated and MIP porosity have an absolute error of 1% and 0.1%, respectively.

Produced (hydrated) density	Total pore volume [mL/g]	MIP porosity [%]	Geometric porosity [%]	Geometric/MIP
hydrated particles				
82	0.0808	14.6	18	1.2
91	0.0196	3.9	9	2.3
99	0.0109	2.2	1	0.5
dehydrated particles				
85	0.1697	24.0	35	1.5
90	0.1212	20.0	30	1.5
98	0.0984	17.4	27	1.6

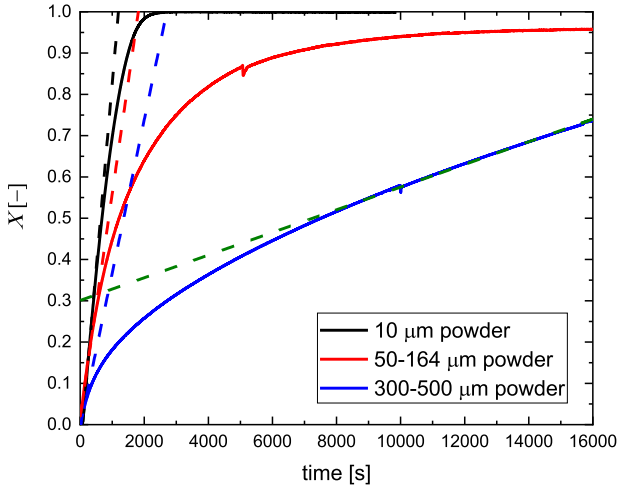

Fig. 8. Hydration conversion versus time for 10, 50-164 and 300-500 ***μm*** powder hydrated at 20°C and 7.7 mbar (33% RH). The dashed lines correspond to the fit using Eq. (6) with zero porosity, the black, red, and blue dashed line were fitted to the initial slope while the dashed green line was fitted to the in final slope of the curve.

$mm^2 \cdot s^{-1}$ and D_{eff} is 0.1 $mm^2 \cdot s^{-1}$ respectively.

In the absence of fragmentation during particle manufacturing, the reaction front is expected to broaden with increasing primary powder size. The computed values indicate that even if this will be the case, the front width is still narrower than the overall particle thickness, which is in the order of 2 mm (Fig. 9). Since in the analyzed particles fragmentation of the base powder has occurred, the real front width will be determined by the powder particle size inside the mm-sized particle.

4.3. The influence of possible edge effects on hydration kinetics

Since the particles used during this study are cylindrical with a finite diameter and height, there could be deviations from flat-plate (1D) behavior due to water vapor transport from the sides. To investigate the effect of water vapor transport from the sides experiments with particles made from 300-500 μm base powder and different relative densities were studied. Half of the particles were hydrated, within 33% relative humidity at 20 °C, with uncovered edges and the other half of the particles had sealed off edges using parafilm. Caution was taken to not cover the top part of the particle with parafilm. The resulting conversion versus time data was fitted to an equation of the form

$$X = \sqrt{qt}. \tag{32}$$

Here q [min^{-1}] denotes the rate constant which is plotted versus particle density in Fig. 10. Fitting was performed without including the data points at and close to 100% conversion since the exact time data point for full conversion could not be determined. To confirm that parafilm was effective at sealing the particles, one particle was completely sealed in parafilm. This particle showed a conversion of only 0.07% in 24 hours.

No significant difference in rate constant for unsealed and sealed particles is visible. This indicates that water vapor transport from the sides is insignificant compared to water vapor transport from the top. Two possible reasons for this could be inhomogeneities in the particle structure and anisotropy in diffusion coefficients.

It is observed by Busignies and coworkers that cylindrical pressed particles suffer from inhomogeneities in their structure (Busignies, 2006) [31]. They found that the density of such particles increases near the edges of the cylinder (porosity decreases). This denser layer near the edge could hamper water vapor transport trough these sides.

An anisotropy in pore direction which can give rise to an anisotropy in diffusion coefficients (tortuosity's) was observed by Wu and coworkers (Wu, 2005) [32]. They found an anisotropy in pore orientation within NaCl pressed cylinders along the compaction direction. This anisotropy in pore orientation could also hinder water vapor transport from the sides in the salt particles used in this work.

In the case of isotropic pore directions and a perfectly homogenous structure, the effective diffusion coefficient is equal to both the effective diffusion coefficient perpendicular and parallel to the top surface so that $D_{eff} = D_{eff}^{\perp} = D_{eff}^{\parallel}$. When anisotropy in pore orientation and inhomogeneity in the structure occurs, which is most probably the case in this work, the effective diffusion coefficients reported are only equal to the effective diffusion coefficient perpendicular to the top surface so that $D_{eff} = D_{eff}^{\perp} \neq D_{eff}^{\parallel}$.

Both denser outer layer and anisotropy in pore orientation could play

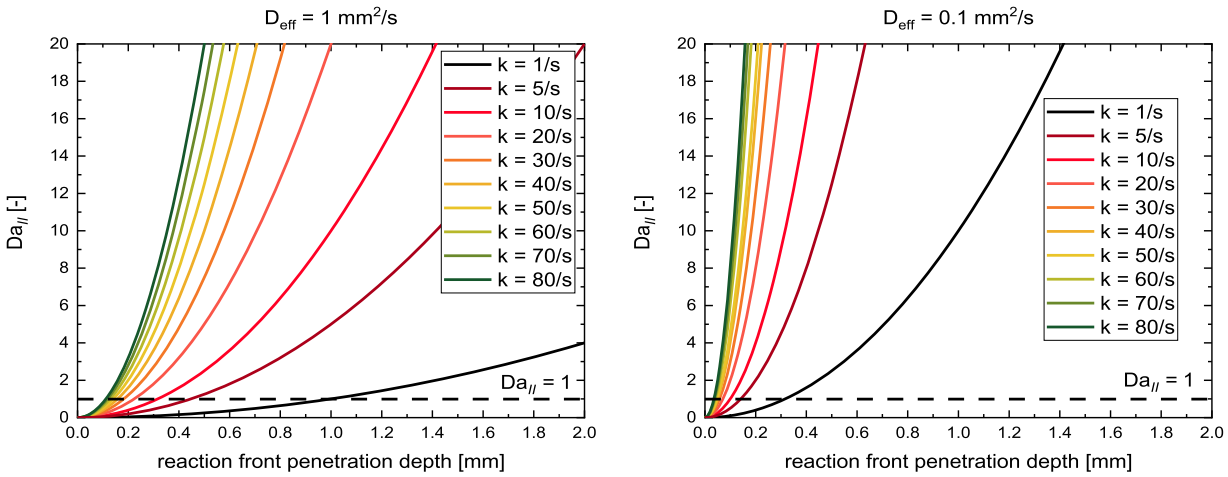

Fig. 9. Second Dämkohler number versus typical lengths with different values for the rate constant. For the calculations, a diffusion coefficient inside the particle of 1 mm^2/s (left) and 0.1 mm^2/s (right) is used. These values correspond to values found later in this work. The rate constant of 80 s^{-1} corresponds to the value found from TGA measurements on 10 μm powder. The dotted line corresponds to a Dämkohler number of one, indicating the moment when diffusion through the particle becomes rate limiting.

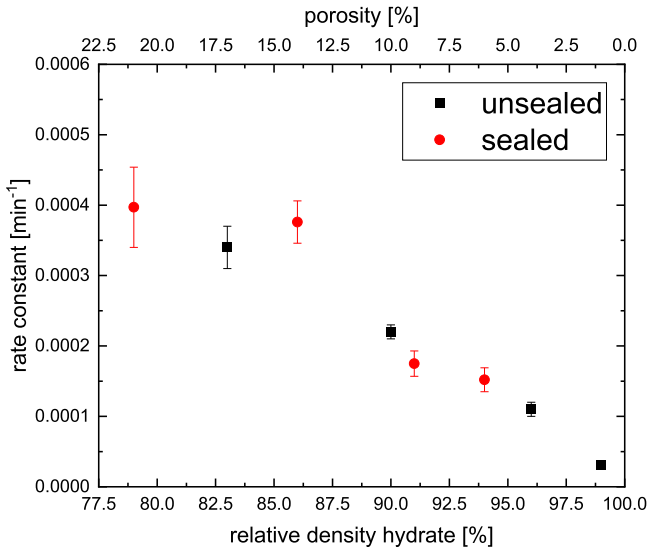

Fig. 10. Rate constant versus particle density (as produced) for particles made from 300-500 μm base powder with sealed and unsealed edges using parafilm.

a role in limiting water vapor transport from the sides in cylindrical salt hydrate particles. Additional sealing did not affect kinetics, and consequently, further discussion will be based on experiments with unsealed particles.

4.4. Effect of particle density and porosity on hydration kinetics

Since different manufacturing pressures result in particles with different densities in hydrated and dehydrated state, the effect of these different densities (porosities) on the kinetic behavior was investigated. The conversion of particles made from 10 μm powder was measured over time (within 33% relative humidity at 20 °C). Afterwards the conversion X was converted into a penetration depth by multiplying with the cylindrical particle height L using Eq. (33) (Fig. 11)

$$f = XL. \tag{33}$$

The penetration depth data was fitted using Eq. (22). The output from these fits resulted in an effective diffusion coefficient of water vapor during hydration (Fig. 11). Fitting was performed without including the data points at and close to 100% conversion (last black square in the penetration depth in Fig. 11). Exclusion of the datapoints at and close to 100% conversion was done to limit the influence of end effects. The other samples did not reach such high conversions.

The reaction rate depends on the density of the pressed hydrated particle. A lower density shows faster kinetics, and the reaction front moves faster throughout the particle. This matches with the data in Fig. 5 showing that particles with higher densities in the hydrated state have higher densities in the anhydrous state.

Since the kinetics varies with density, the diffusion of water vapor through the particles has to vary with density as well, as can be seen in Fig. 11. The resulting effective diffusion coefficients are in the same range of water vapor diffusion coefficient in air at 20 °C (24.2 $mm^2 \cdot s^{-1}$) [33].

With the availability of D_{eff} a range of tortuosity values can be estimated using the following equation [34]:

$$D_{eff} \equiv \frac{D_{air} \cdot \varepsilon_{hyd}}{\tau}. \tag{34}$$

Here τ [−] is the tortuosity being the ratio of the real and theoretical (shortest) path length, D_{air} [$mm^2 \cdot s^{-1}$] is the diffusion coefficient of water vapor in air and ε_{hyd} [−] the porosity of the hydrated phase. Here the hydrated salt porosity (as produced) is used since diffusion of water vapor proceeds through the product (hydrated salt) layer. During hydration the internal structure of the particle is constantly changing. As a result, the porosity will most likely vary from a value smaller to a value larger than the initial porosity over time (conversion) as well. The used hydrated porosity (as produced) therefore resembles an approximate average value.

The resulting tortuosity values are found to be within a range of 2 till 7 (Fig. 12). Lower porosity corresponds to higher tortuosity values (and lower D_{eff}) since the effective path length increases. The pore diameter decreases for less porous particles (MIP), which results in a shorter mean free path for water molecules before hitting the pore walls.

Various theoretical models exist for describing tortuosity in porous media. These models rely on the main assumption that the primary grains whereof the porous media is constructed are perfectly spherical. A few of these models predicting high and low values of tortuosity are given and displayed in Fig. 12. For other available models the reader is referred to the corresponding references.

The first model by Lanfrey (2009), is based on a packed bed of uniformly sized spheres (red line in Fig. 12) [35]. Two different models derived by Arkany (1987) which are based on Monte Carlo simulations

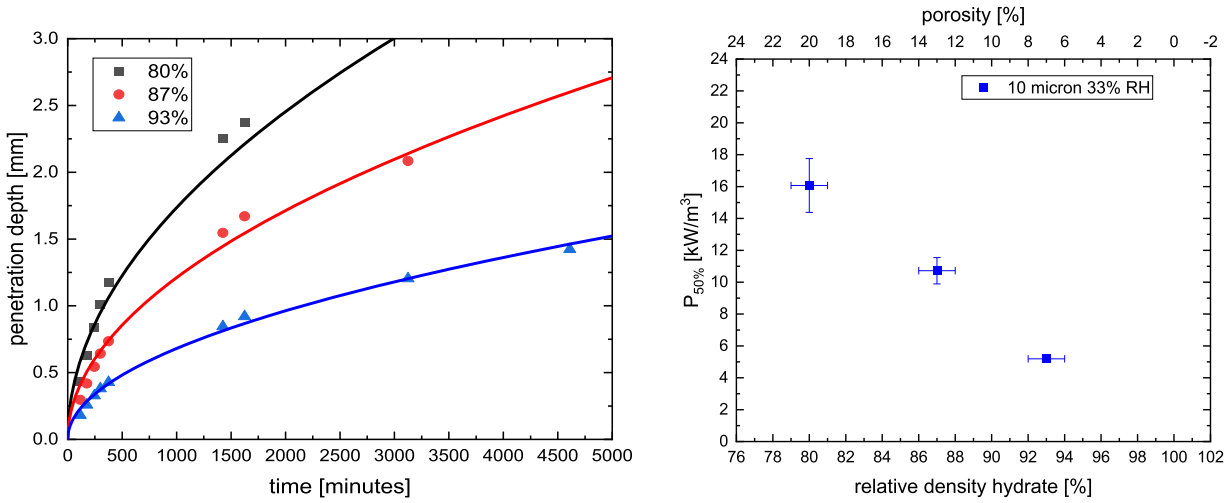

Fig. 11. Penetration depth versus time plot for particles made from 10 ***μm*** powder with different relative densities of the hydrated particle. Fitting was performed using Eq. (22). Particles were hydrated at 33% relative humidity and 20°C. Only data points below 100% conversion are shown since the exact time of reaching 100% conversion could not be determined. The solid lines correspond to the fitted curves (left). Effective diffusion coefficients for particles made from 10 ***μm*** powder with different relative densities of the hydrated particles (right).

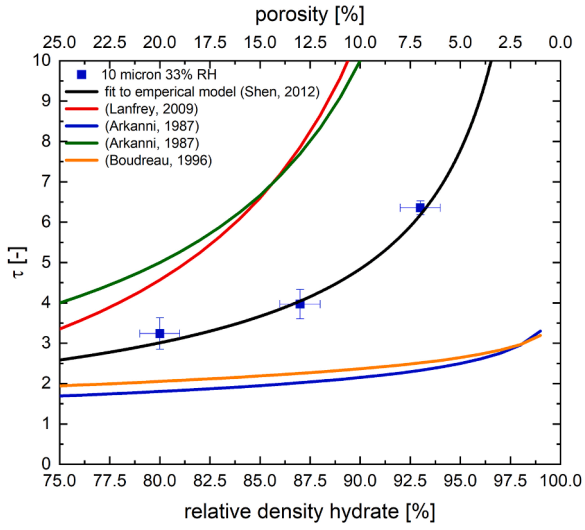

Fig. 12. Estimated tortuosity values for particles made from 10 ***μm*** powder with different relative densities of the hydrated particles. Particles were hydrated at 33% relative humidity and 20°C. The solid black line corresponds to the empirical fit mentioned in the work of Shen (2007) [38] . The other solid lines correspond to different theoretical models [35,36,37].

are given representing the green and blue line in Fig. 12 respectively [36]. The last model presented here by Boudreau (1996) is based on the fine grained unlithified sediments (orange line in Fig. 12) [37].

Additional theoretical and empirical relationships between tortuosity and porosity are summarized by Shen (2007) [38]. The found tortuosity values gave the best fit using the empirical model for tortuosity in sand and mud:

$$\tau = \sqrt{\left(A \cdot \varepsilon_{\mathrm{hyd}}^{1-B}\right)^{C}}. \tag{35}$$

Here A [−], B [−] and C [−] represent the fit parameters. The values of A and C were fixed at 1 as was done in the work of Shen as well [38]. This resulted in a B value of 2.37 $\pm$ 0.01. The exact magnitude of the coefficient is greatly determined by the precise structure of the porous material. The fact that the model for sand and mud works well is not rather unexpected since a pressed particle is a random configuration of grains with varying grain sizes, just like sand. As seen in Fig. 12 the found tortuosity values and the empirical fit lay in between the values predicted using the theoretical models.

4.5. *Effect of primary powder size on hydration kinetics*

Additionally, the effect of powder size on hydration kinetics was investigated. Apart from 10 μm powder, particles made from two other powder fractions were experimentally testes. The studied fractions were 50-164 μm and 300-500 μm, respectively. To be able to make a proper comparison, these particles were dehydrated and hydrated under the same conditions as particles made from 10 μm powder. The penetration depths versus time curves are show in Fig. 13. Again, Fitting was performed without the data point at and close to 100% conversion (last black square for 50-164 μm, final 3 black squares for 300-500 μm and final red circle in Fig. 13) using Eq. (22). Exclusion of the datapoints at and close to 100% conversion was done to limit the influence of end effects. The other samples did not reach such high conversions.

The particles made from the 50-164 μm and 300-500 μm fractions show similar behavior as observed in the particles of 10 μm powder with respect to density. To compare, the effective water vapor diffusion coefficient for each particle was extracted from the fit and the results are shown in Fig. 14. Comparing the effective diffusion coefficients of all particles shows that the diffusion coefficient at certain hydrated densities is independent of the used powder size.

Even though powder hydration kinetics varies significantly with size, fragmentation during particle fabrication most probably causes the base powder to fragment into smaller particles. These fragmented particles have sufficiently high rate constants resulting in diffusion limited kinetics not sensitive to the primary powder size.

This confirms that the hydration process of K_2CO_3 particles is mainly diffusion limited. The hydration kinetics are therefore not limited by the actual hydration reaction itself, but by the diffusion of water vapor towards the reaction front. As a result, the main parameter for controlling the kinetics here is the (initial) density (porosity) at which the particle is produced.

For the application of salt particles in thermochemical heat storage the performance of a particle should be assessed by means of the power output. In this work the average power output per volume at 50% conversion is used. The advantage of focusing on both the effective diffusion coefficient and power output is that the first gives information on the transport phenomena and the latter is a real indicator of particle

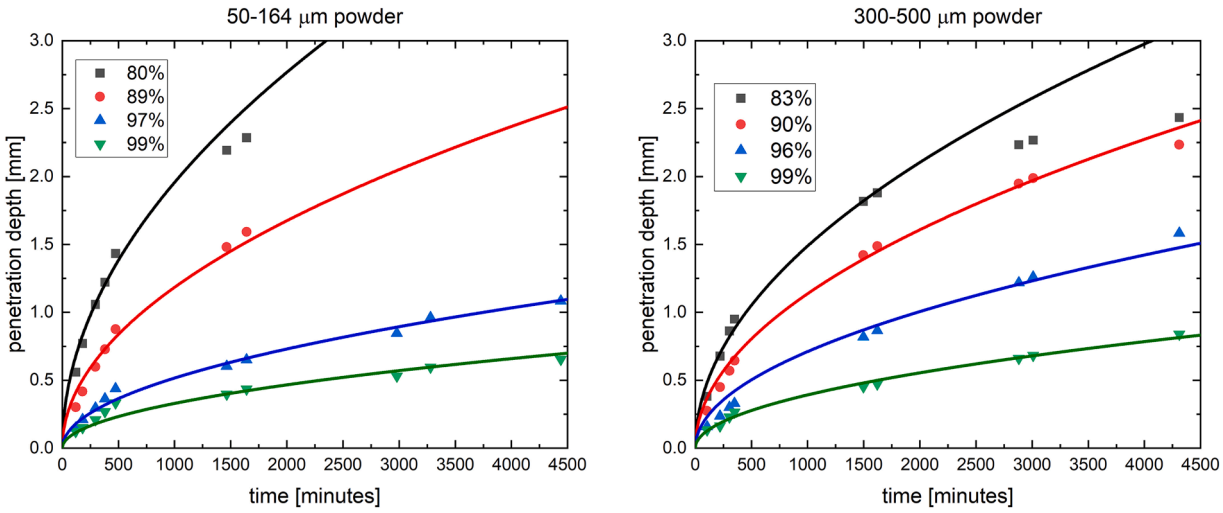

Fig. 13. Penetration depth versus time plots for particles made from 50-164 ***μm*** (left) and 300-500 ***μm*** (right) powder with different relative densities of the hydrated particles. Fitting was done using Eq. (22). Particles were hydrated at 33% relative humidity and 20°C. Only data points below 100% conversion are show since the exact time of reaching 100% conversion could not be determined. The solid lines correspond to the fitted curves.

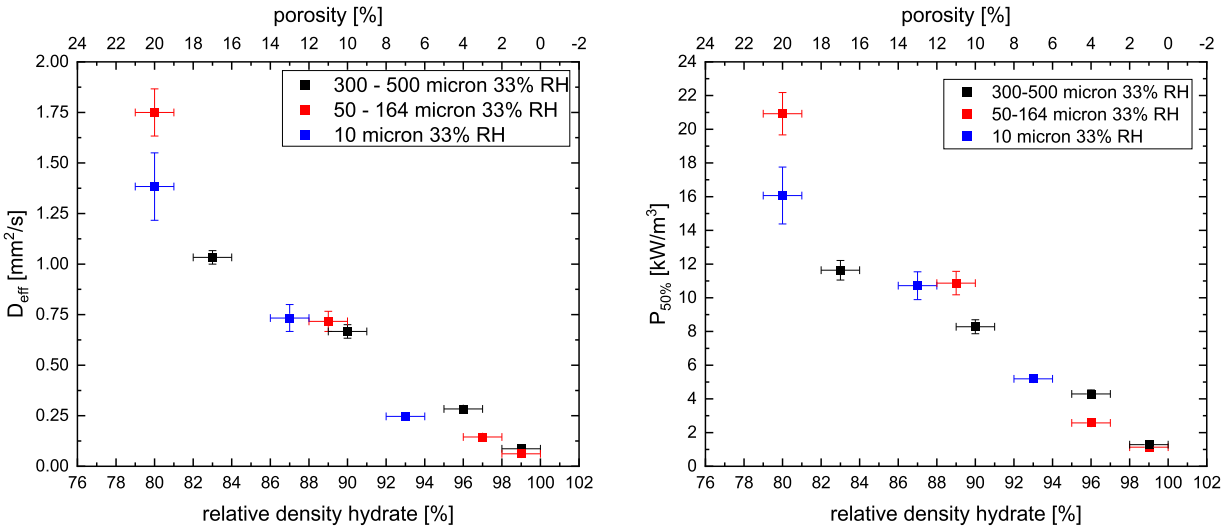

Fig. 14. Diffusion coefficient for various powder sizes (left) and power at 50% conversion (right) at different hydrated densities.

performance. The average power output per volume at 50% conversion $P_{50\%}$ [W·m^{-3}] is defined using the following equation

$$P_{50\%} = \frac{N_{\text{water}} \cdot \Delta H}{t_{50\%} \cdot V_0}. \tag{38}$$

Here N_{water} [mol] represents the reacted moles of water at 50% conversion, $t_{50\%}$ [s] the time it takes to reach 50% conversion, ΔH the reaction enthalpy and V_0 [m^3] the total volume of the produced particle. For particles which did not reach 50% conversion in the measured time, the data was extrapolated to find $t_{50\%}$. In Fig. 14 one can see that the power output is not influenced by the powder particle size just like the effective diffusion coefficients. The density is influencing the power output because the diffusion of water vapor is also density dependent. A smaller diffusion coefficient results in a slower front speed and therefore longer $t_{50\%}$.

4.6. *Effect of driving force on hydration kinetics*

Since particle hydration is diffusion limited, this will have implications on how the kinetics are affected by changing the driving force. In case of a reaction limited process obeying first order kinetics, the hydration rate (and therefore conversion) is expected to scale linearly with driving force (as in Eq. (6)). From Eq. (22) it follows that conversion and penetration depth for a diffusion limited process scales with the square root of the driving force. Therefore, lower penetration depths are expected for lower driving force.

Even though the conversion scales with the square root of the driving force, the effective diffusion coefficients are expected to be independent of driving force. To verify the statements made, cylindrical particles made from 300-500 μm powder were hydrated under 22% and 11% relative humidity. The resulting penetration depth versus time graphs are show in Fig. 15. Again, fitting was performed using Eq. (22). Exclusion of the datapoints at and close to 100% conversion was not necessary, since the samples did not reach such high conversions.

The same trend with respect to densities is observed when hydrating at lower driving forces. The lower a particle density is, the faster the particle hydrates. Comparing the two graphs in Fig. 15 already shows a lower penetration depth for lower relative humidity's for particles made with comparable density. This is an indication for decreased water vapor flux towards the reaction front and with that a decreased front velocity.

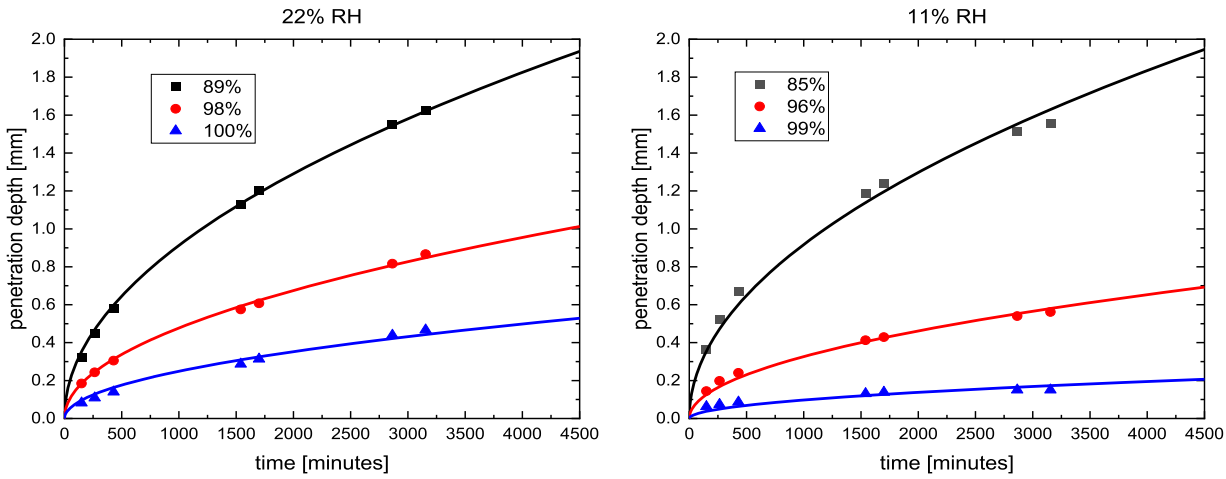

Fig. 15. Penetration depth versus time plots for particles made from 300-500 ***μm*** powder with different relative densities of the hydrated particles. Particles were hydrated at 22% (left) and 11% (right) relative humidity and 20°C. Only data points below 100% conversion are show since the exact time of reaching 100% conversion could not be determined. The solid lines correspond to the fitted curves using Eq. (22).

Since the effective diffusion coefficient is a constant which depends on density but not on driving force, the resulting diffusion coefficient from fitting Eq. (22) is expected to be similar for comparable densities. Obtained values for D_{eff} for experiments performed at different RH-values are plotted in Fig. 16. From Fig. 16 it is observed D_{eff} is indeed independent of driving force.

Now the effective diffusion coefficient as function of relative density can be fitted to a polynomial equation of the form $D_{\text{eff}} = A + B\rho_{\text{rel}} + C\rho_{\text{rel}}^2$. In the limit that $\rho_{\text{rel}} = 0$, D_{eff} must be equal to the theoretical diffusion coefficient for water vapor in air (24.2 $\text{mm}^2\cdot\text{s}^{-1}$ at 20 °C [33]). Therefore $A = 24.2\ \text{mm}^2\cdot\text{s}^{-1}$ and the equation takes the form $D_{\text{eff}} = 24.2 + B\rho_{\text{rel}} + C\rho_{\text{rel}}^2$. The other limit at which $\rho_{\text{rel}} = 100\ \%$, $D_{\text{eff}} = 0$. Applying these boundary conditions results in $B = (-0.451 \pm 0.006)\ \text{mm}^2\cdot\text{s}^{-1}\cdot\%^{-1}$ and $C = (0.0021 \pm 0.0001)\ \text{mm}^2\cdot\text{s}^{-1}\cdot\%^{-2}$.

In contrast to the effective diffusion constant, which is unaffected by the water vapor pressure, the power output is influenced by the driving force (Fig. 16). The power for particles hydrated at 22% RH is lower than that for particles hydrated at 33% RH, and for particles hydrated at 11% RH the power output is lower than for particles hydrated at 22% RH. This is clearly visible in Fig. 16 in which the slope of the linear fits is decreasing with decreasing driving force.

The reason for the lower power output at lower relative humidity is due to the lower pressure gradient. The flux towards the reaction front is lower and the partial water vapor pressure inside the pores will decrease. Because the concentration of water in the pores is lower, the time to fully hydrate a slice of salt at the reaction front increases and the power output decreases.

It can be concluded that the mechanism of water vapor transport (vapor diffusion) inside the particle is unaffected by the driving force, but the power output in contrast is. The water vapor transport is only a function of density since the effective diffusion coefficient is only affected by changes herein. The power output is also a function of driving force.

4.7. Parameterization of different geometries

To predict the influence of the geometry of a particle on the hydration kinetics, similar solutions like Eq. (19) can be obtained for the geometry of a cylinder (2D, only transport from the curved sides) and a sphere (3D) respectively [21]:

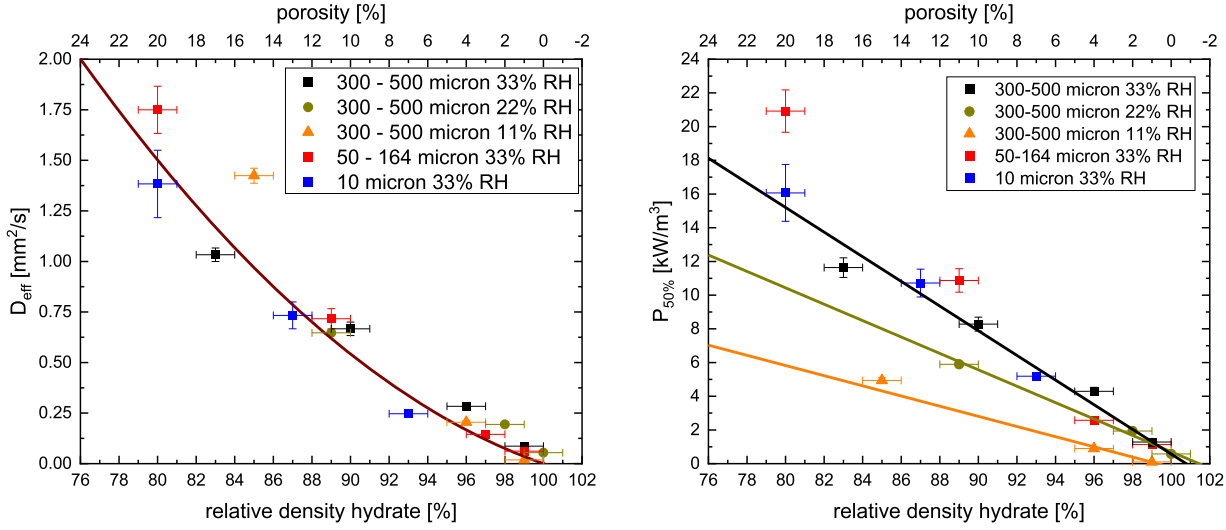

Fig. 16. Effective diffusion coefficient (left) and power at 50% conversion (right) for various base powder sizes at different hydrated densities and relative humidity's. The solid line in the left image corresponds to the fitted curve of the form $\boldsymbol{D_{eff} = 24.2 + B\rho_{rel} + C\rho_{rel}^2}$. The solid lines in the right picture correspond to the linear fit for particles made with 300-500 ***μm*** powder. The black, green, and orange line correspond to 33% 22% and 11% RH respectively.

$$4\cdot\frac{M_s\cdot(c_0-c_{eq})}{b\cdot\rho_s\cdot(1-\varepsilon)}\cdot\frac{D_{eff}}{L^2}\cdot t = X+(1-X)\ln(1-X), \tag{37}$$

$$6\cdot\frac{M_s\cdot(c_0-c_{eq})}{b\cdot\rho_s\cdot(1-\varepsilon)}\cdot\frac{D_{eff}}{L^2}\cdot t = 1+2(1-X)-3(1-X)^{2/3}. \tag{38}$$

Note that these equations hold under the assumption that the diffusivity is constant (homogeneous density distribution) and isotropic. Keeping this assumption mind, the obtained 1D diffusion constants can be used for first estimates of the kinetics of cylindrical and spherical shaped particles. The conversion curves for different shapes with the same typical length scale are displayed in Fig. 17. For a flat plate (Eq. (19)) L represents the thickness, for an infinitely long cylinder (Eq. (37)) and sphere (Eq. (38)) it represents the radius. For a fair comparison of all three geometries the pre factor was given the same value and set to 1 (similar volume and porosity).

$$\frac{M_s\cdot(c_0-c_{eq})}{b\cdot\rho_s\cdot(1-\varepsilon)}\cdot\frac{D_{eff}}{L^2}=1. \tag{39}$$

For the flat plate it is assumed no hydration occurs from the side and for cylinder hydration only occurs through the curved sides. It is clearly visible that curved shapes with similar volume, porosity, homogeneous structure, and isotropic diffusion constant favor the hydration speed of the particles and that these shapes can be parameterized using the results from this work.

The difference in kinetics can be best seen when comparing the time for 50% conversion indicated by the dashed lines in Fig. 17. It is found that the time for 50% conversion decreases when the number of dimensions increases $t_{50\%,\ 3D} = 0.48t_{50\%,\ 2D} = 0.15t_{50\%,\ 1D}$. This change in $t_{50\%}$ influences the power output as can be seen in Fig. 18.

The underlying reason for this increase in kinetics upon increasing the dimension can be found in the surface to volume ratio (SA/V ratio). A larger SA/V ratio allows for faster hydration since it results in a larger exposed surface trough which water vapor can diffuse compared to the reacting volume. The surface area to volume ratio for the 1D, 2D and 3D systems in Fig. 17 are equal to $1/L$, $2/L$ and $3/L$ respectively. This show that for particles with similar L the SA/V ratio for multidimensional particles is larger, hence their faster kinetics. For particles with the same dimension the dimensional size is important as well. Decreasing the dimensional size by decreasing L results in a higher SA/V ratio. Therefore, from a kinetic point of view an infinitesimal spherical particle (powder) is therefore desired. From the reactor concept point of view a larger particle is desired. Where the optimum between size, shape, kinetics, and bed permeability resides must be investigated in future studies.

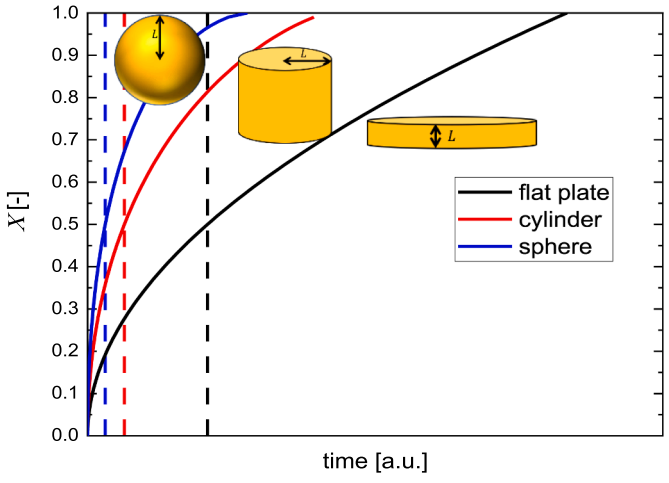

Fig. 17. Conversion versus time for arbitrary chosen particles with different geometries. The dashed lines represent the time for 50% conversion.

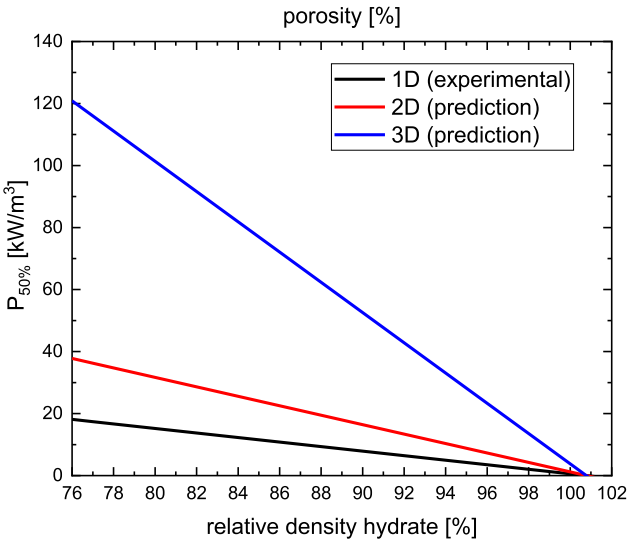

Fig. 18. Linear fit of the experimentally calculated power output from Fig. 16 for a 1D system (black line) and predicted values for equal particles as if they would be 2D (red line) or 3D (blue line).

5. Conclusion

In this work it is shown for the first time that the hydration kinetics of mm-sized K_2CO_3 particles is a diffusion limited process. The hydration rate is limited by the supply of water vapor towards the reaction front instead of the actual reaction at the salt. The existence of such a reaction front was illustrated by using kinetic data from powder measurements. The width of this front is linked to the diffusion inside the pores and the reaction rate at the primary powder. Fast diffusion results in a broader front while slow diffusion results in a narrower front. Due to fragmentation of the base powder during particle manufacturing, reaction front widths much smaller than the particle size were obtained.

Since the hydration kinetics are diffusion limited, the particle density and porosity are found to be the key particle parameters affecting the power output of such mm-sized salt hydrate particles. The tortuosity calculated from the found effective diffusion coefficients was found to follow the empirical expression used to describe the tortuosity in sand and mud. Lower porosities resulted in lower effective diffusion coefficients and higher tortuosity values. This higher tortuosity was due to particles with lower porosities having pores with smaller diameters.

Investigating the effect of driving force on the hydration behavior showed that the transport mechanism is insensitive to changes in driving force and only a material property. The power output on the other hand is affected by changes in driving force.

The calculated effective diffusion coefficients using the model presented in this work can be used to predict kinetic behavior of particles with other geometries (2D and 3D). Calculations showed that the power output can be enhanced by changing the dimensionality or size of the particle. Since the particle hydration mechanism is expected to be similar for salts with comparable or faster reaction rate constants, the model used in this work is applicable to different combinations of shapes and salts. As a follow up, the results from this work can be used to design and investigate other particles made from various thermochemical materials and shapes. Adding to that, an in-depth investigation into possible diffusion anisotropy or inhomogeneities in the particle pore structure must be conducted. Lastly, finding the optimal configuration between kinetics, size, shape, and bed permeability could be of interest.

To the best knowledge of the authors, no analytical solutions have yet been derived for sharp front diffusion models with other geometries than flat plate, cylindrical and spherical. For the investigation of more complicated geometries, numerical analysis is thus required. The numeric models can then again be parameterized using the results from

this work.

Funding

This project has received funding from the European Unions Horizon 2020 research and innovation program under grant agreement No 869810. This work reflects only the author's view. The European Commission is not responsible for any use that may be made of this information.

CRediT authorship contribution statement

Joey Aarts: Conceptualization, Methodology, Writing – original draft, Visualization, Investigation. **Stan de Jong:** Conceptualization, Methodology, Writing – original draft, Visualization. **Martina Cotti:** Conceptualization, Writing – review & editing, Investigation. **Pim Donkers:** Conceptualization, Writing – review & editing. **Hartmut Fischer:** Conceptualization, Writing – review & editing. **Olaf Adan:** Conceptualization, Writing – review & editing, Supervision, Funding acquisition. **Henk Huinink:** Conceptualization, Writing – review & editing, Supervision, Funding acquisition.

Declaration of Competing Interest

The authors declare that they have no known competing financial interests or personal relationships that could have appeared to influence the work reported in this paper.

Acknowledgements

The authors would like to thank Hans Dalderop for his technical support, Natalia Mazur for performing TGA experiments on powder samples, Peter Lipman for MIP measurements and Evonik Functional Solutions GmbH for providing the potassium carbonate salt.

References

[1] X. Cao, X. Dai, J. Liu, Building energy-consumption status worldwide and the state-of-the-art technologies for zero-energy buildings during the past decade, Energy Build 128 (2016) 198–213, https://doi.org/10.1016/j.enbuild.2016.06.089.
[2] F. Belaïd, Understanding the spectrum of domestic energy consumption: Empirical evidence from France, Energy Policy 92 (May 2016) 220–233, https://doi.org/10.1016/j.enpol.2016.02.015.
[3] A. E. Brooks, "Solar Energy," in *Future Energy*, Elsevier, 2014, pp. 383–404.
[4] D. Infield, "Wind Energy," in *Future Energy*, Elsevier, 2014, pp. 313–333.
[5] E. Guy, Solar Heat Storage Using Chemical Reactions, J. Solid State Chem. 22 (1977) 51–61.
[6] K. Kaygusuz, The Viability of Thermal Energy Storage, Energy Sources 21 (8) (Aug. 1999) 745–755, https://doi.org/10.1080/00908319950014489.
[7] P.A.J. Donkers, L.C. Sögütoglu, H.P. Huinink, H.R. Fischer, O.C.G. Adan, A review of salt hydrates for seasonal heat storage in domestic applications, Appl. Energy 199 (Aug. 2017) 45–68, https://doi.org/10.1016/j.apenergy.2017.04.080.
[8] L.C. Sögütoglu, P.A.J. Donkers, H.R. Fischer, H.P. Huinink, O.C.G. Adan, In-depth investigation of thermochemical performance in a heat battery: Cyclic analysis of K2CO3, MgCl2 and Na2S, Appl. Energy 215 (no. January) (Apr. 2018) 159–173, https://doi.org/10.1016/j.apenergy.2018.01.083.
[9] M. Gaeini, S.A. Shaik, C.C.M. Rindt, Characterization of potassium carbonate salt hydrate for thermochemical energy storage in buildings, Energy Build 196 (Aug. 2019) 178–193, https://doi.org/10.1016/j.enbuild.2019.05.029.
[10] R. Fisher, Y. Ding, A. Sciacovelli, Hydration kinetics of K2CO3, MgCl2 and vermiculite-based composites in view of low-temperature thermochemical energy storage, J. Energy Storage 38 (March) (2021), 102561, https://doi.org/10.1016/j.est.2021.102561.
[11] L.-C. Sögütoglu, et al., Understanding the Hydration Process of Salts: The Impact of a Nucleation Barrier, Cryst. Growth Des. 19 (4) (Apr. 2019) 2279–2288, https://doi.org/10.1021/acs.cgd.8b01908.
[12] L.C. Sögütoglu, F. Birkelbach, A. Werner, H. Fischer, H. Huinink, O. Adan, Hydration of salts as a two-step process: Water adsorption and hydrate formation, Thermochim. Acta 695 (May 2020), 178819, https://doi.org/10.1016/j.tca.2020.178819. Jan. 2021.
[13] M.A. Stanish, D.D. Perlmutter, Kinetics of hydration-dehydration reactions considered as solid transformations, AIChE J 30 (4) (Jul. 1984) 557–563, https://doi.org/10.1002/aic.690300405.
[14] M.A.J.M. Beving, A.J.H. Frijns, C.C.M. Rindt, D.M.J. Smeulders, Effect of cycle-induced crack formation on the hydration behaviour of K2CO3 particles: Experiments and modelling, Thermochim. Acta 692 (no. March) (Oct. 2020), 178752, https://doi.org/10.1016/j.tca.2020.178752.
[15] B. Michel, N. Mazet, S. Mauran, D. Stitou, J. Xu, Thermochemical process for seasonal storage of solar energy: Characterization and modeling of a high density reactive bed, Energy 47 (1) (2012) 553–563, https://doi.org/10.1016/j.energy.2012.09.029.
[16] Z.H. Pan, C.Y. Zhao, Gas–solid thermochemical heat storage reactors for high-temperature applications, Energy 130 (Jul. 2017) 155–173, https://doi.org/10.1016/j.energy.2017.04.102.
[17] D.D. Wagman, et al., The NBS Tables of Chemical Thermodynamic Properties, J. Phys. Chem. Ref. Data 11 (Feb. 1982), 125007, https://doi.org/10.6028/jres.125.007.
[18] A.D. Rubio, A. Zalts, C.D. El Hasi, Numerical solution of the advection–reaction–diffusion equation at different scales, Environ. Model. Softw. 23 (1) (Jan. 2008) 90–95, https://doi.org/10.1016/j.envsoft.2007.05.009.
[19] B.S. Sampath, P.A. Ramachandran, R. Hughes, Modelling of non-catalytic gas-solid reactions-I. Transient analysis of the particle-pellet model, Chem. Eng. Sci. 30 (1) (Jan. 1975) 125–134, https://doi.org/10.1016/0009-2509(75)85123-2.
[20] I. Stakgold, K.B. Bischoff, V.V. Gokhale, Validity of the pseudo-steady-state approximation, Int. J. Eng. Sci. 21 (5) (Jan. 1983) 537–542, https://doi.org/10.1016/0020-7225(83)90101-5.
[21] J. Szekely, J. W. Evans, and H. Y. Sohn, "Reactions of Porous Solids," in *Gas-solid Reactions*, J. Szekely, J. W. Evans, and H. Y. B. T.-G. R. Sohn, Eds. Elsevier, 1976, pp. 108–175.
[22] A. Khawam, D.R. Flanagan, Solid-State Kinetic Models: Basics and Mathematical Fundamentals, J. Phys. Chem. B 110 (35) (Sep. 2006) 17315–17328, https://doi.org/10.1021/jp062746a.
[23] W.E. Garner, Chemistry of the Solid State, Butterworths Scientific Publications, London, 1955.
[24] P. Villars and K. Cenzual, Eds., "K2CO3•1.5H2O (K4[CO3]2[H2O]3) Crystal Structure: Datasheet from 'PAULING FILE Multinaries Edition –2012' in SpringerMaterials (https://materials.springer.com/isp/crystallographic/docs/sd_0377610)." Springer-Verlag Berlin Heidelberg & Material Phases Data System (MPDS), Switzerland & National Institute for Materials Science (NIMS), Japan, [Online]. Available: https://materials.springer.com/isp/crystallographic/docs/sd_0377610.
[25] P. Villars and K. Cenzual, Eds., "K2CO3 (K2[CO3] rt mon1) Crystal Structure: Datasheet from 'PAULING FILE Multinaries Edition –2012' in SpringerMaterials (https://materials.springer.com/isp/crystallographic/docs/sd_1215403)." Springer-Verlag Berlin Heidelberg & Material Phases Data System (MPDS), Switzerland & National Institute for Materials Science (NIMS), Japan, [Online]. Available: https://materials.springer.com/isp/crystallographic/docs/sd_1215403.
[26] H.A. Al-Qureshi, A. Galiotto, A.N. Klein, On the mechanics of cold die compaction for powder metallurgy, J. Mater. Process. Technol. 166 (1) (Jul. 2005) 135–143, https://doi.org/10.1016/j.jmatprotec.2004.08.009.
[27] S. Chikosha, T.C. Shabalala, H.K. Chikwanda, Effect of particle morphology and size on roll compaction of Ti-based powders, Powder Technol 264 (2014) 310–319, https://doi.org/10.1016/j.powtec.2014.05.033.
[28] M. Frenning, G., "Compression Mechanics of Powders and Granular Materials Probed by Froce Distributions and Micromechanicaly Based Compaction Equation.," *Igarss* 2014, vol. 159, no. 1, pp. 1–5, 2014.
[29] H.P. Kurz, G. Münz, The influence of particle size distribution on the flow properties of limestone powders, Powder Technol 11 (1) (Jan. 1975) 37–40, https://doi.org/10.1016/0032-5910(75)80020-9.
[30] K.W. Desmond, E.R. Weeks, Influence of particle size distribution on random close packing of spheres, Phys. Rev. E 90 (2) (Aug. 2014), 022204, https://doi.org/10.1103/PhysRevE.90.022204.
[31] V. Busignies, B. Leclerc, P. Porion, P. Evesque, G. Couarraza, P. Tchoreloff, Quantitative measurements of localized density variations in cylindrical tablets using X-ray microtomography, Eur. J. Pharm. Biopharm. 64 (1) (Aug. 2006) 38–50, https://doi.org/10.1016/j.ejpb.2006.02.007.
[32] Y.S. Wu, H.W. Frijlink, L.J. van Vliet, I. Stokroos, K. van der Voort Maarschalk, Location-Dependent Analysis of Porosity and Pore Direction in Tablets, Pharm. Res. 22 (8) (Aug. 2005) 1399–1405, https://doi.org/10.1007/s11095-005-5280-x.
[33] D.R. Lide, G. Baysinger, CRC Handbook of Chemistry and Physics, CRC Press, 2016.
[34] L.M. Pismen, Diffusion in porous media of a random structure, Chem. Eng. Sci. 29 (5) (May 1974) 1227–1236, https://doi.org/10.1016/0009-2509(74)80122-3.
[35] P.-Y. Lanfrey, Z.V. Kuzeljevic, M.P. Dudukovic, Tortuosity model for fixed beds randomly packed with identical particles, Chem. Eng. Sci. 65 (5) (Mar. 2010) 1891–1896, https://doi.org/10.1016/j.ces.2009.11.011.
[36] K.A. Akanni, J.W. Evans, I.S. Abramson, Effective transport coefficients in heterogeneous media, Chem. Eng. Sci. 42 (8) (1987) 1945–1954, https://doi.org/10.1016/0009-2509(87)80141-0.
[37] B.P. Boudreau, The diffusive tortuosity of fine-grained unlithified sediments, Geochim. Cosmochim. Acta 60 (16) (Aug. 1996) 3139–3142, https://doi.org/10.1016/0016-7037(96)00158-5.
[38] L. Shen, Z. Chen, Critical review of the impact of tortuosity on diffusion, Chem. Eng. Sci. 62 (14) (Jul. 2007) 3748–3755, https://doi.org/10.1016/j.ces.2007.03.041.